CRYSTAL GROWTH & DESIGN

pubs.acs.org/crystal

Article

Structural Properties and Charge Redistribution in Cocrystallized Pharmaceutical Ingredients: A Comparative Experimental and Theoretical Charge Density Analysis

Camila B. Pinto, Adilson B. Wanderley, Juan C. Tenorio, Ihosvany Camps, Christian W. Lehmann, and Javier Ellena*

Cite This: *Cryst. Growth Des.* 2024, 24, 5614−5626

Read Online

ACCESS | Metrics & More | Article Recommendations | Supporting Information

ABSTRACT: The cocrystallization of active pharmaceutical ingredients (APIs) is known to be a technique suitable for overcoming certain physicochemical issues concerning the solid forms of drugs. In the case of the cocrystal of 5-fluorocytosine and isoniazid, two widely used active pharmaceutical ingredients, for example, the cocrystallization improved the phase stability of the latter against moisture, thus increasing its shelf life. The room-temperature crystal structure was already reported in the literature, but no charge density study has been published so far. To further evaluate the structural properties of this potential codrug, which is stabilized by a supramolecular synthon containing N−H···N-type hydrogen bonds, here we performed the experimental and theoretical charge density analyses of the drug−drug cocrystal formed by the antimetabolite prodrug 5-fluorocytosine and the tuberculostatic drug isoniazid. Topological analyses were also performed for all models and compared, indicating a good agreement between experiment and theory. The comparison with gas-phase calculations enabled the evaluation of the charge redistribution upon cocrystallization as well as the effect of the intermolecular interactions. In this manner, it was possible to evaluate the variations in bond distances and electron densities at the bonds involved in the intermolecular heterosynthon. Through the total charge of each molecule in the cocrystal, it was also possible to have insights into the charge redistribution when both molecules crystallize together. Electrostatic potential maps were also calculated for the experimental data and compared with the gas-phase calculations.

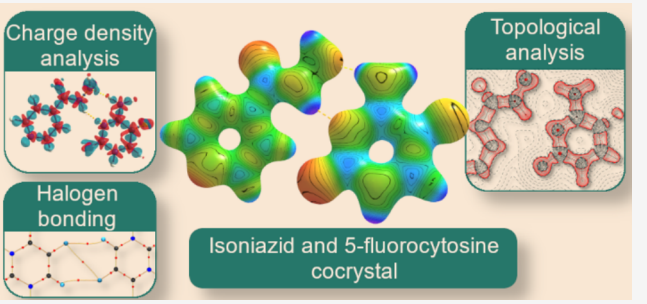

INTRODUCTION

Pharmaceutical cocrystals have received much attention, both in the pharmaceutical industry and in the scientific community, due to their advantages in relation to pure active pharmaceutical ingredients (APIs). Among these advantages, one can mention the enhanced pharmaceutical performance, greater stability and shelf life, optimization of the manufacturing process, patents, and intellectual property.[1] Within this framework, drug−drug cocrystals are a special type involving the presence of two or more APIs in the crystallographic asymmetric unit linked by intermolecular interactions, thus preserving their neutral character without breaking or forming covalent bonds and maintaining their effectiveness.[2,3] The recognition and manipulation of the supramolecular synthons are the key aspects to successfully design these kinds of solid forms.[4] However, only a few cases of drug−drug cocrystals have been reported in the literature because drug−drug cocrystals are considered fixed-dose combination products,[5] and hence, the APIs involved need to be those which are usually coadministered, also presenting a proper dosage.[6]

The properties of active pharmaceutical ingredients (APIs) in the solid state are determined by their functional groups as well as the intra- and intermolecular interactions, which will be responsible for molecular recognition processes in biological systems.[5] In this regard, the knowledge of structural and electronic aspects of new solid forms is crucial for the understanding of structure−property relationships and reactivity. In a previous work, the room-temperature crystal structure of the 5-fluorocytosine and isoniazid drug cocrystal (5FC:INH) was reported.[7] Isoniazid (INH, Figure 1a) is an antibiotic drug widely used for the treatment of tuberculosis[8] and 5-fluorocytosine (5FC, Figure 1b) is an antifungal medication.[9] Both APIs are usually administered orally, and the cocrystallization process improved the stability against moisture for the INH molecule. The cocrystal crystallizes in the triclinic space group $P\bar{1}$, with one molecule of 5FC

Received: March 19, 2024
Revised: June 7, 2024
Accepted: June 10, 2024
Published: June 17, 2024

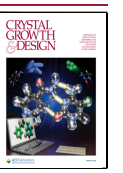

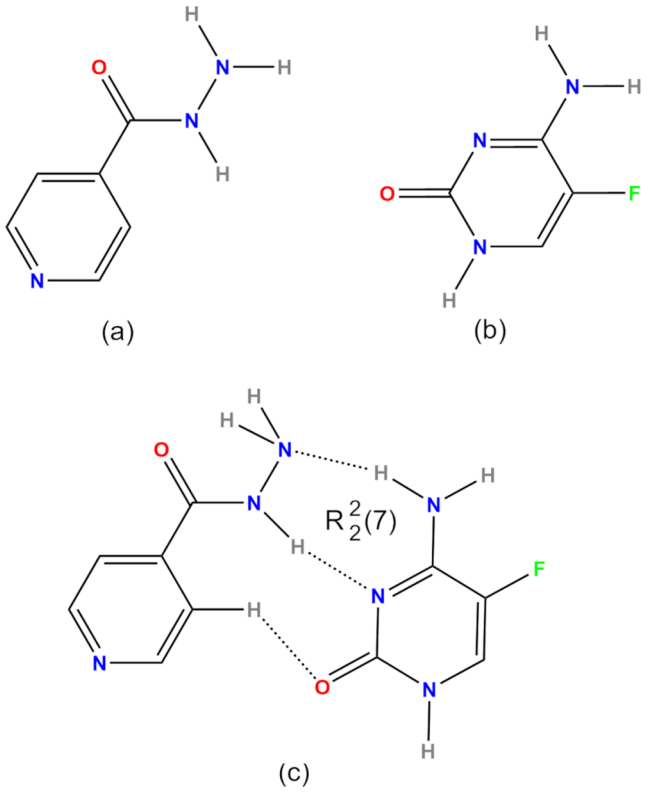

Figure 1. Schematic representation of the chemical structure of (a) isoniazid, (b) 5-fluorocytosine, and (c) the cocrystal (5FC:INH), showing the $R_2^2(7)$ synthon.

interacting with one molecule of INH through H-bonds. The result of this interaction is the formation of a supramolecular synthon (Figure 1c), consisting of N−H···N interactions between the amine and imine fragments of the 5FC ring with the *N*-hydrazide atoms of the INH molecule, forming a $R_2^2(7)$ motif.[10] However, a discussion on the supramolecular conformation or the electronic structure was not performed since the study by Souza and co-workers[7] focused on the cocrystal obtention by mechanochemical methods.

In this context, here we describe the experimental and theoretical charge density study, along with topological analysis based on Bader's quantum theory of atoms in molecules (QTAIM),[11] of the pharmaceutical cocrystal 5FC:INH to determine and quantify the features of its electronic distribution as well as to evaluate the nature of the intermolecular interactions responsible for the cocrystal stability. At the same time, this analysis allows us to understand the role that each atom and chemical bond plays in the structure. Gas-phase calculations for the cocrystal and the individual molecules were also performed, enabling an evaluation of the charge redistribution upon cocrystal formation and of the electronic modifications due to the intermolecular interactions responsible for the crystal structure packing.

EXPERIMENTAL SECTION

The synthesis of the cocrystal followed the methodology reported in the literature,[7] and good-quality single-crystals were obtained by slow evaporation of the solvent.

Data Collection. Intensity data were collected on a Bruker AXS Kappa APEX II CCD diffractometer based on a Mach3 goniometer. The radiation source was an INCOATEC I-μS microsource emitting Mo−Kα radiation, equipped with INCOATEC Helios MX focusing optics. An Oxford Cryosystem 700 controller was also used to ensure temperature stability during data collection, which was set to 150 K. For high-resolution X-ray diffraction data collection, measurements were carried out using ω scans of 0.5° width at different θ detector angle settings and different counting time conditions (inner shell: 10 s and redundancy 8, middle shell: 20 s and redundancy 6, and outer shell: 120 s and redundancy 6). For each detector setting, several runs with different crystal rotations Φ were registered. Data integration was performed using SAINT software.[12] Absorption corrections based on multiple observations were performed using SADABS software.[12] Further details on data collection can be found in Table 1.

Table 1. Data Collection and Refinement Details of the 5FC:INH Cocrystal

crystal data	
chemical formula	$C_{10}H_{11}N_6O_2F$
M_r	266.25
crystal system, space group	triclinic, $P\bar{1}$
a, *b*, *c* (Å)	3.6833 (2), 9.6484 (5), 16.3512 (8)
α, β, γ (deg)	76.068 (2), 88.936 (2), 81.425 (2)
V (Å^3)	557.60 (5)
Z	2
crystal dimensions (mm)	0.21 × 0.11 × 0.03
density (calculated) (mg m^{-3})	1.586
data collection	
temperature	150.0(2)
μ (mm^{-1})	0.128
no. of measured, independent, and observed reflections	274 732, 16 950, 9659
R_{int}	0.0895
$(\sin\theta/\lambda)_{max}$ (Å^{-1})	1.25
refinement	
independent atom model refinement (IAM)	
$R(F^2)$, $wR(F^2)$ ($I > 2\sigma(I)$), GooF	0.056, 0.146, 1.019
no. of reflections	16 950
no. of parameters	217
$\Delta\rho_{max}$,$\Delta\rho_{min}$ (e Å^{-3})	0.97, −0.48
multipole model refinement (MM)	
$R(F^2)$, $wR(F^2)$, GooF[a]	0.033, 0.045, 1.529
no. of reflections/included in the refinement	16945/6122
no. of parameters	524
$\Delta\rho_{max}$,$\Delta\rho_{min}$ (e Å^{-3})	0.159, −0.184

[a]These statistics are calculated considering only the reflections which are considered in the refinement. See the text for details.

Independent Atom Model Refinement. The structure was solved initially by direct methods with the SHELXS program[13] using the independent atom model (IAM) method. The refinement was based on F^2 for all reflections using SHELXL.[14] Weighted *R* factors (*wR*) and the goodness-of-fit (*S*) values are based on F^2. The $F_o^2 > 2\sigma(F_o^2)$ criterion was used only for calculating *R* factors, and it is not relevant to the choice of the reflections during the refinement. Anisotropic displacement parameters were freely refined for all non-H atoms. H atoms were refined isotropically in the first stages against low-resolution intensity data in order to determine their positions in the difference Fourier map and to assess the U_{eq} vibrational parameters and were subsequently refined against all data. The program suites *Olex2*[15] and WinGX-2016[16] were used for the structure solution and visualization of the initial models. For the refinement and assessment of the IAM electron density, the ShelXle[17] program, a graphical user interface for SHELX, was used.

Multipole Refinement. The initial atomic coordinates and anisotropic parameters for the multipole refinement were taken

https://doi.org/10.1021/acs.cgd.4c00401
Cryst. Growth Des. 2024, 24, 5614−5626

from the IAM refinement. An experimental aspherical multipolar refinement based on the Hansen & Coppens model[18] was performed using the XDLSM module of the XD2006 program suite.[19] In this model, the pseudoatoms are defined by eq 1, where the atomic densities are represented by the spherical core ρ_c and the valence ρ_v along with a term accounting for the deformation valence density. The normalized Slater-type radial function, the corresponding multipole population, and the density-normalized real spherical harmonic functions expressed in polar coordinates are represented, respectively, by R_l, $P_{lm\pm}$, and $d_{lm\pm}$. The expansion−contraction coefficients of the spherical part κ and the deformation valence densities κ' are given in the last two terms, respectively.

$$\rho(\boldsymbol{r}) = P_c\rho_c(\boldsymbol{r}) + P_v\kappa^3\rho_v(\kappa\boldsymbol{r}) + \sum_{l=0}^{l_{max}} \kappa'^3 R_l(\kappa'\boldsymbol{r}) \sum_{m=0}^{l} P_{lm\pm} d_{lm\pm}(\theta, \varphi) \quad (1)$$

The least-squares multipole refinement was based on F^2. Furthermore, the cutoff based on resolution was a necessary condition for the success of the refinement, given that the reflections at the highest resolution shell ($\sin\theta/\lambda > 1.2$ Å^{-1}) caused severe instability on the refinement. In this way, the included reflections were those lying in the resolution range of $0.1 < (\sin\theta/\lambda_{Mo}) < 1.0$ Å^{-1}. In addition, a cutoff based on the observations was included, considering observations higher than 2. The cutoff in reflections significantly improved the final statistics, which were $R(F) = 0.1208$ and $R(F^2) = 0.0503$ when considering all data. The multipole expansion was truncated at the hexadecapole level ($l_{max} = 4$) for the F atom and at the octupole level for the rest of the nonhydrogen atoms ($l_{max} = 3$), while only a bond-directed dipole ($l_{max} = 2$) was refined for H atoms. The atoms were assumed to have no local symmetry. Anisotropic displacement parameters for H atoms in the cocrystal were estimated by the SHADE-2.1 program,[20] which is known to provide an excellent approximation for H atom ADPs.[21] Meanwhile, hydrogen atom positions were restrained to neutron-derived distances with a deviation value $\sigma = 0.001$ Å, based on the averaged values reported by Allen & Bruno,[22] during the IAM refinement, and they were kept fixed in those values during the multipole refinement. Each pseudoatom was assigned a core and spherical valence scattering factor based on Clementi's Hartree−Fock wave functions, while valence deformation functions used a single-ζ Slater-type radial function multiplied by the density-normalized spherical harmonics.

The radial fit for the chemically distinct atoms was optimized by the refinement of their expansion−contraction parameters κ and κ'. The κ' parameter was refined for N and C atoms from the 5FC molecule and C(7I) from INH (see Figure 2 for atom labeling). It is noteworthy that chemical equivalence constraints were applied for the refinement of the κ and κ' parameters so that values for C and N atoms with the same hybridization are equal. In the meantime, the κ and κ' coefficients for the H atoms were restrained to the values of 1.130 and 1.200, respectively.[23]

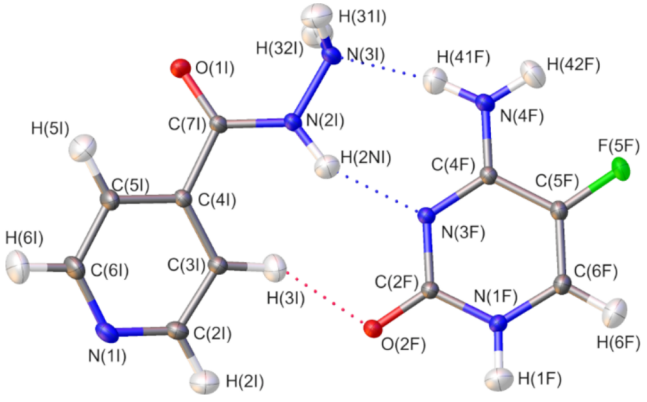

Figure 2. Asymmetric unit for 5FC:INH at 150 K, with a labeling scheme, showing the heterosynthon. Ellipsoids are drawn at 50% probability.

To assess the coherent behavior of the thermal motion, the Hirshfeld rigid bond test was performed. This test determines that refined ADPs are deemed to be physically meaningful if differences of mean-squared displacement amplitudes (DMSDAs) along interatomic vectors are $\leq 1 \times 10^{-3}$ Å^2 (Table S1). Likewise, to confirm the quality of the refined model, scatter plots of the scale factor (F_{obs}/F_{calc}) against sin θ/λ (resolution), normal probability plots, and fractal dimension plots (Meindl-Henn plots) were analyzed[24,25] (Figure S1). The residual electron density maps are featureless, as confirmed by the fractal dimension plots.

The program packages XDPROP, TOPXD, and WinPROP were used for the topological analysis of the total electron density.[18] The topological descriptors were obtained for the asymmetric unit, generating equivalent atoms when necessary. The charges were calculated in TOPXD, considering the entire crystal. The program MoleCoolQt[26] was employed to visualize some topological properties and to plot isosurfaces.

Theoretical Calculations and Computational Details. Quantum mechanical calculations on periodic systems were performed with the CRYSTAL14 set of programs[27] using the density functional theory (DFT), with the B3LYP level of theory[28,29] and the 6-311++G** basis set to determine the single-point energy. The 5FC:INH cocrystal information for single-point calculations was obtained from the multipolar refinement of the single-crystal X-ray diffraction data. For the coulomb and exchange integrals, the following parameters were used: ITOL1 = ITOL2 = ITOL3 = ITOL4 = 7 and ITOL5 = 14. The shrinkage factor along the reciprocal lattice was set to 8, corresponding to 260 k points in the Brillouin irreducible zone. The geometry was then optimized at the same level of theory. Theoretical calculations in nonperiodic systems were performed with the GAUSSIAN09 set of programs[30] using DFT at the B3LYP level of theory and the 6-311++G** basis set. The geometry of the structures for the individual molecules (model IV) was also optimized at the B3LYP/6-311++G** level of theory.

Topological descriptors for the theoretical data were calculated using the TOPOND code package[31] for periodic systems. Maps of gradient trajectories, bond paths, and contour maps were also constructed using the TOPOND code. Multiwfn[32] and AIMAll[33] programs were used to perform topological analysis for nonperiodic systems and to calculate the electrostatic potential maps.[34]

In summary, the study of the charge density distributions including the topological analysis calculations was carried out using four different models: (I) multipolar refinement of the experimental data; (II) theoretical model for solid-state calculation on the periodic system; (III) theoretical model for the gaseous state of the 5FC:INH cocrystal; and (IV) theoretical model for the gaseous state of 5FC and INH molecules separately.

RESULTS AND DISCUSSION

Crystal Structure. The crystal structure of 5FC:INH at 150 K is illustrated in Figure 2. Refinement details can be found in Table 1 and the geometric parameters for the H-bonds are reported in Table 2 and will be further discussed through topological analysis. Even though the H atom positions were not refined in the multipole refinement, they were allowed to vary within an interval during the IAM refinement; therefore, the D−H distance values listed in Table 2 present standard deviations associated with them. The two molecules in the cocrystal are connected via H-bonds between the amine and imine fragments from the 5FC molecule and the hydrazide group from INH. A weak nonclassic H-bond between the oxygen atom from 5FC and the aromatic ring in INH is also present. These three H-bonds are similar to those formed by the cytosine nucleobase with guanine in DNA, and hence, it is referred as pseudo-Watson−Crick bonding in 5FC:INH. The three-dimensional packing of the crystal

https://doi.org/10.1021/acs.cgd.4c00401
Cryst. Growth Des. 2024, 24, 5614−5626

Table 2. Geometric Parameters for H-Bonds in 5FC:INH[a]

D−H···A	D−H (Å)	H···A (Å)	D···A (Å)	D···A (deg)
N(4F)−H(41F)···N(3I)	1.0096(5)	1.9530(4)	2.9516(6)	170.92(1)
N(2I)−H(2NI)···N(3F)	1.0280(4)	2.0464(4)	3.0059(6)	154.29(2)
C(3I)−H(3I)···O(2F)	1.0814(4)	2.4958(6)	3.1920(7)	121.13(3)
N(1F)−H(1F)···O(2F)^{i}	1.0293(4)	1.6963(4)	2.7233(6)	172.37(1)
N(3I)−H(31I)···O(1I)^{ii}	1.0229(5)	2.1739(5)	2.9499(7)	131.21(3)
N(3I)−H(32I)···O(1I)^{iii}	1.0235(6)	2.1373(7)	3.1140(9)	158.90(3)
N(4F)−H(42F)···N(1I)^{iv}	1.0098(4)	1.9661(4)	2.9228(5)	157.09(3)
C(3I)−H(3I)···N(3F)^{v}	1.0814(4)	2.5563(4)	3.4605(6)	140.58(3)
C(6F)−H(6F)···F(5F)^{vi}	1.0815(4)	2.4222(6)	3.3137(7)	138.84(3)

[a]Symmetry operations: (i) 1−*x*,2−*y*,−*z*; (ii) 1−*x*,2−*y*,1−*z*; (iii) −*x*,2−*y*,1−*z*; (iv) 1+*x*,1+*y*,*z*; (v) −1+*x*,*y*,*z*; and (vi) 2−*x*,3−*y*,-*z*.

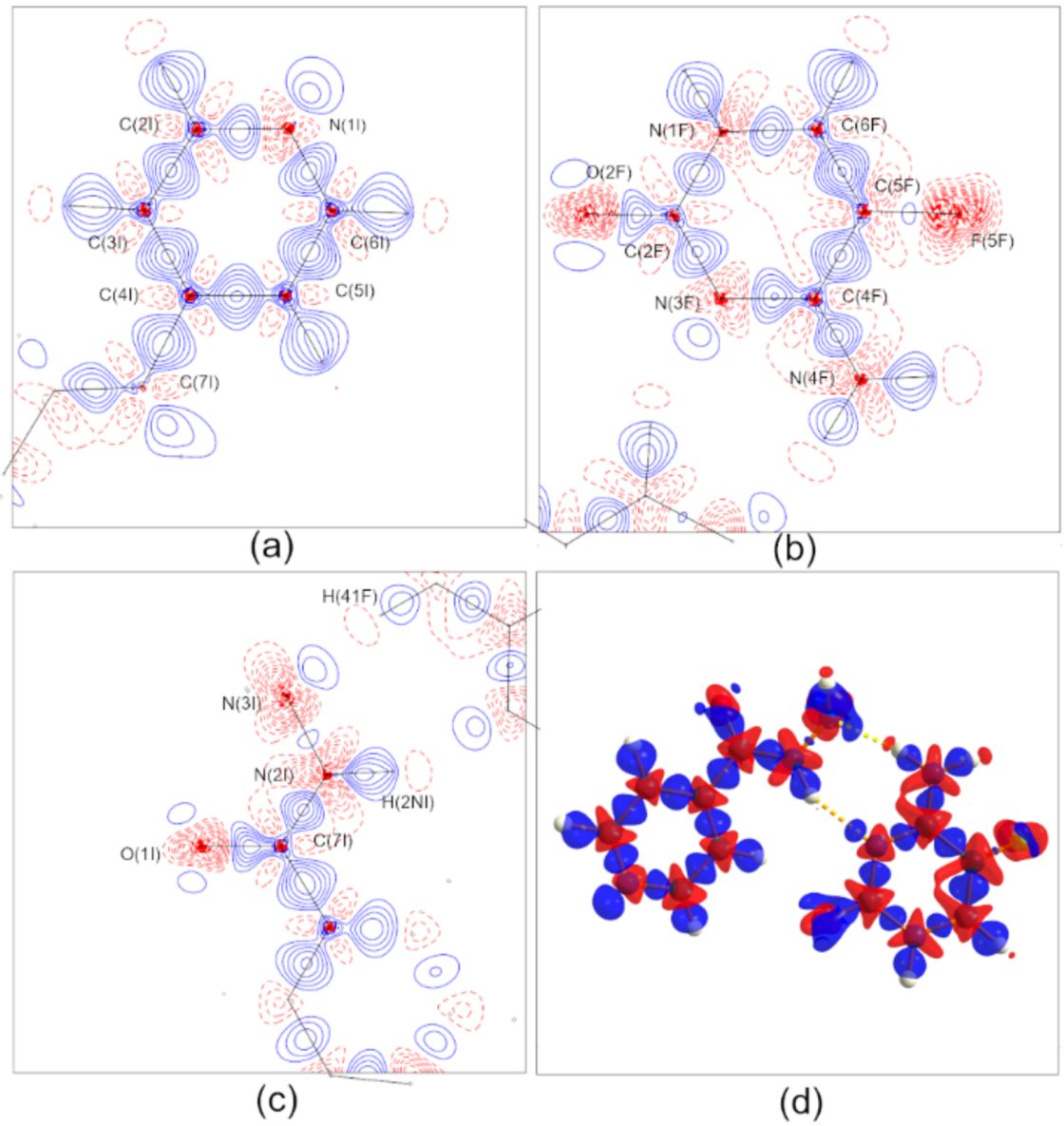

Figure 3. Experimental static deformation density showing (a) the pyridine ring of INH, (b) the 5FC molecule, (c) the hydrazide group of INH and the heterosynthon, and (d) the deformation density isosurface of the cocrystal. Contours were at 0.1 e Å^{-3}. Blue solid lines are positive contours and red dashed lines are negative contours. Isosurfaces are drawn at −0.15 and +0.125 au, blue: positive, red: negative.

structure is also stabilized by H-bonds, as demonstrated in Figure S3.

Charge Density Analysis. The statistical refinement parameters obtained after multipole refinement are considerably better than those obtained after IAM refinement, as can be seen in Table 1. The experimental static deformation density maps (Figure 3) also confirm the quality of the model since density accumulation can be seen in regions related to

https://doi.org/10.1021/acs.cgd.4c00401
Cryst. Growth Des. 2024, 24, 5614−5626

covalent bonds and lone pairs. It is possible to observe the formation of a synthon through the interaction of regions of charge accumulation (nitrogen lone pairs) and charge depletion (in red, close to H atoms) (Figure 3c). The deformation density isosurface (Figure 3d) shows the F lone pairs above and below the molecular plane, not visible through the contour map. Furthermore, the deformation density maps indicate a low charge accumulation in the N(2I)−N(3I) and C(5F)−F(5F) bonds, in comparison to the other covalent bonds in the cocrystal. The same feature is observed for the N−N bond from the INH molecule in a charge density study conducted by Rajalakshmi and co-workers[35] and for C−F in other compounds from the literature (*e.g.* refs 36 and 37).

Topological Analysis. The electron density obtained after multipole refinement can be partitioned according to the quantum theory of atoms in molecules (QTAIM), which allows the evaluation of topological descriptors at the bond critical points (BCPs) and throughout the bond path (bp). One advantage of the topological analysis is that it can also be performed on theoretical data, enabling the comparison of experimental and theoretical charge densities. However, small deviations in the position of the bond critical points can cause significant differences in the parameter values, especially those related to second derivatives, such as Laplacian and ellipticity. Furthermore, the position of the bond critical points is influenced by the difference in polarity between the atoms to which the bond critical point is associated, being closer to the less electronegative atom.[38] In this regard, the rule holds the following: the more polar the bond, the higher is the deviation of the bond critical point from the midpoint between the atoms. In the compound under study, the most polar bonds are of type C−O and C−F, so the bond critical points are closer to the carbon atom, as can be seen by the molecular graph (Figure 4), which is the resulting graph from the combination of the critical points and bond paths, and it is associated with a stable molecule.[39] BCPs were found in all of the expected chemical bonds and interactions. Ring critical points were found not only at the center of the pyridine and pyrimidine rings but also at the center of the heterosynthon and at the center of the nine-membered ring formed due to the C(3I)−H(3I)···O(2F) H-bond.

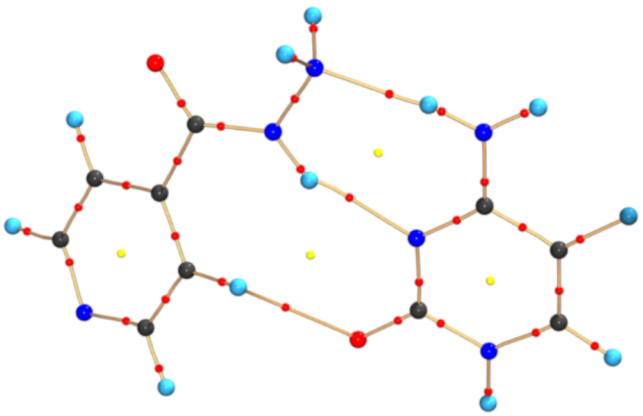

Figure 4. Molecular graph for the cocrystal 5FC:INH for model I. Red dots: bond critical points (3,−1); yellow dots: ring critical points (3,+1); gold lines: bond paths; and colored spheres: (3,−3) critical points associated with the position of C atoms (black), N atoms (blue), F atoms (light blue), O atoms (red), and H atoms (cyan).

The values of the topological descriptors at the bond critical points are shown in Table 3 (covalent interactions) and Table 4 (noncovalent interactions). Overall, there is a good agreement between the electron density at the BCP and the bond length, in which longer (weaker) bonds present lower electron density values, while shorter (stronger) bonds present a higher electron density. The values obtained for the Laplacian of the electron density are consistent with what would be expected. Negative values are obtained for covalent bonds (shared shells) (Table 3), and positive values are obtained for the H-bonds (closed-shell interactions) (Table 4). However, as already stated, small differences in the position of the bond critical point can cause huge deviations in the values of properties based on second derivatives, so discrepancies can be found between experiment and theory. In this sense, a good agreement is seen between experimental and theoretical electron density ($\rho(\mathbf{r}_{BCP})$) descriptors, while there are discrepancies for the Laplacian ($\nabla^2\rho(\mathbf{r}_{BCP})$) and ellipticity ($\varepsilon$)[11] among different models.

Experimentally, the electron density for bonds of the C−N type was found to be between 2.030 and 2.338 e Å^{-3}, in excellent agreement with the values obtained from the periodic calculation (between 2.055 and 2.353 e Å^{-3}) and from the gas-phase calculation (between 2.052 and 2.331 e Å^{-3}), being also quite reasonable with those reported by Rajalakshmi and co-workers[35] for experimental and periodic calculations on INH, as well as for the gas-phase calculations.[40] The values regarding the gas-phase calculation on the 5FC molecule are reasonable with those reported by Murgich and co-workers.[41] A comparison between the isolated model (model IV) and models I, II, and III, which consider the cocrystal, shows an increase in the electron density for the C(2F)−N(1F) (ring), C(2F)−N(3F) (ring), C(7I)−N(2I), and C(4F)−N(4F) bonds, while a small decrease in the electron density is seen in the C(2I)−N(1I) (ring), C(6I)−N(1I) (ring), and C(4F)−N(3F) (ring) bonds. The ellipticity for these bonds is slightly high, indicating a small contribution from the π-electrons. However, as noted by Murgich and co-workers,[41] the ellipticity is not always a reliable parameter for the evaluation of the bond order. For instance, as listed in Table 3, it is possible to observe that an increase of approximately 3% in $\rho(\mathbf{r}_{BCP})$ from N(1F)−C(2F) to N(1F)−C(6F) results in a higher increase in ε when compared to a $\rho(\mathbf{r}_{BCP})$ increase of approximately 11% when going from N(1F)−C(2F) to C(2F)−N(3F).

Both C−O bonds in the cocrystal present a high electron density at the BCP, which, along with the small bond path length (1.24 Å), are interpreted as double bonds, in agreement with the values reported in the literature.[2,35,40−43] Concerning C(2F)═O(2F) from 5FC, there is a good agreement between the experimental electron density and the periodic calculation. The gas-phase calculation, on the other hand, presents a higher electron density, especially considering the isolated 5FC molecule. The lower electron density for the models in which the cocrystal is taken into account is explained by the formation of a weak H-bond between O(2F) and H(3I) in the cocrystal, which causes an elongation of the C═O bond, diminishing the electron density at the BCP. In the C(7I)═O(1I) bond, a carbonyl group belonging to INH, there is a good agreement between experimental and theoretical results, although O(1I) is also involved in H-bonds with neighboring molecules. The values obtained for the C−O bonds are close to those reported in the literature.[2,35,40,42,43]

https://doi.org/10.1021/acs.cgd.4c00401
Cryst. Growth Des. 2024, 24, 5614−5626

Table 3. Topological Properties of the Electron Density in the BCPs for the Relevant Covalent Bonds in 5FC:INH[a]

bond	$\rho(r_{BCP})$ (e Å^{-3})	$\nabla^2\rho(r_{BCP})$ (e Å^{-5})	ε	R_{ij} (Å)
N(1F)−C(2F)	2.030(36)	−19.057(213)	0.129	1.381
	2.055	−21.331	0.129	1.390
	2.052	−20.262	0.102	1.382
	1.876	−17.787	0.105	1.426
N(1F)−C(6F)	2.084(38)	−21.012(207)	0.229	1.360
	2.141	−20.778	0.091	1.359
	2.128	−20.333	0.100	1.360
	2.130	−20.494	0.106	1.360
C(2F)−O(2F)	2.500(41)	−17.354(268)	0.245	1.247
	2.595	−11.782	0.095	1.247
	2.636	−14.356	0.122	1.247
	2.796	−8.527	0.124	1.215
C(2F)−N(3F)	2.249(33)	−31.469(147)	0.180	1.360
	2.260	−25.063	0.143	1.355
	2.235	−24.733	0.121	1.360
	2.167	−23.3807	0.109	1.376
C(4F)−N(3F)	2.301(32)	−29.413(133)	0.275	1.340
	2.296	−25.412	0.109	1.344
	2.330	−25.625	0.134	1.340
	2.439	−27.062	0.144	1.315
C(4F)−N(4F)	2.338(42)	−30.884(239)	0.189	1.324
	2.353	−24.952	0.168	1.322
	2.331	−23.862	0.138	1.323
	2.191	−22.796	0.129	1.352
C(4F)−C(5F)	2.028(27)	−22.986(82)	0.295	1.431
	1.995	−19.544	0.218	1.434
	2.002	−19.713	0.212	1.432
	1.978	−19.151	0.221	1.438
C(5F)−F(5F)	1.782(32)	−11.528(184)	0.250	1.352
	1.626	4.409	0.096	1.363
	1.684	4.380	0.082	1.352
	1.656	3.759	0.097	1.359
C(5F)−C(6F)	2.315(33)	−29.858(109)	0.539	1.347
	2.295	−24.455	0.421	1.346
	2.306	−24.655	0.432	1.344
	2.289	−24.316	0.429	1.348
N(1I)−C(2I)	2.251(50)	−25.315(262)	0.340	1.333
	2.292	−22.381	0.106	1.334
	2.314	−23.283	0.104	1.333
	2.308	−23.716	0.105	1.336
N(1I)−C(6I)	2.256(58)	−21.624(311)	0.190	1.343
	2.274	−22.704	0.106	1.340
	2.285	−23.491	0.104	1.341
	2.294	−23.520	0.100	1.339
C(2I)−C(3I)	2.125(22)	−24.337(61)	0.295	1.393
	2.110	−21.336	0.197	1.392
	2.107	−21.256	0.199	1.392
	2.098	−21.001	0.210	1.394
C(3I)−C(4I)	2.122(25)	−25.233(83)	0.270	1.389
	2.093	−20.900	0.185	1.391
	2.106	−21.157	0.188	1.388
	2.069	−20.379	0.191	1.397
C(4I)−C(5I)	2.126(22)	−22.819(61)	0.333	1.392
	2.086	−20.856	0.187	1.395
	2.105	−21.291	0.184	1.390
	2.084	−20.798	0.185	1.395
C(4I)−C(7I)	1.828(25)	−16.821(72)	0.204	1.496
	1.764	−15.711	0.088	1.501
	1.769	−15.785	0.086	1.499
	1.750	−15.146	0.084	1.505
C(5I)−C(6I)	2.178(24)	−25.080(69)	0.308	1.387
	2.131	−21.661	0.213	1.386
	2.129	−21.629	0.211	1.387
	2.110	−21.265	0.204	1.392
C(7I)−N(2I)	2.227(62)	−26.329(429)	0.212	1.341
	2.233	−22.931	0.166	1.347
	2.235	−21.865	0.127	1.342
	2.133	−22.105	0.140	1.371
C(7I)−O(1I)	2.700(94)	−31.804(610)	0.177	1.236
	2.621	−8.317	0.045	1.238
	2.662	−9.238	0.058	1.235
	2.734	−6.684	0.084	1.221
N(3I)−N(2I)	1.995(21)	−5.902(59)	0.058	1.408
	2.139	−12.685	0.008	1.409
	2.133	−12.627	0.016	1.411
	2.140	−12.664	0.025	1.409

[a] $\rho(r_{BCP})$ is the electron density at the bond critical point, $\nabla^2\rho(r_{BCP})$ is the Laplacian of the electron density at the bond critical point, ε is the ellipticity, and R_{ij} is the bond path length. Line one: model I; line two: model II; line three: model III, and line four: model IV.

The electron density value at the N(2I)−N(3I) BCP is in agreement with the one reported by Rajalakshmi[35] for INH. Interestingly, the small negative value for the Laplacian observed for the INH molecule[35] (−5.7 e Å^{-5}) was also observed for the cocrystal (−5.9 e Å^{-5}), which indicates a weak bond. This is in agreement with the deformation density map (Figure 3), which shows a small charge accumulation in the N(2I)−N(3I) bond. The theoretical values for the Laplacian, on the other hand, are slightly more negative (around −12 e Å^{-5}) than those found for the INH molecule[35] (approximately −6 e Å^{-5}), but are in agreement with those reported for the gas-phase calculations.[40]

The C(5F)−F(5F) bond has an electron density value lower than the other covalent bonds in the cocrystal (1.7 e Å^{-3} on average) along with a small negative Laplacian value for the experiment, as visible through the deformation density maps (Figure 3), while low positive Laplacian values were obtained in the theoretical calculations, which would indicate a closed-shell interaction. For the reported gas-phase calculation,[41] a small Laplacian value is also found for this bond (−0.87 e Å^{-5}). However, an evaluation of the Laplacian profile throughout the bond path demonstrates a good agreement with the experimental values (Figure 5). In addition, the Laplacian profile is characteristic of a polar covalent bond, with the valence shell charge concentration (VSCC) of both atoms belonging to the atomic basin of the most electronegative atom. The Laplacian profile for this bond differs from that of an ionic bond especially in the region between the VSCCs, which, in the case of an ionic bond, presents a large flat positive region containing the BCP.[44] An interesting feature of the Laplacian profiles, as shown in Figure 5a, is that the regions of the VSCC for the isolated molecule and for the cocrystal are almost coincident, while in that for the polar C−O bond (Figure 5b), the VSCC closer to the O atom is shifted to higher R_{ij} (the distance between nuclear critical points of atoms i and j) values in the cocrystal due to the elongation of the bond caused by the formation of a weak H-bond.

https://doi.org/10.1021/acs.cgd.4c00401
Cryst. Growth Des. 2024, 24, 5614−5626

Table 4. Topological Properties of the Electron Density in the BCP of H-Bond Interactions in the Cocrystal[a]

bond	$\rho(r_{BCP})$	$\nabla^2\rho(r_{BCP})$	ε	R_{ij}	$V(r)$	$G(r)$	$H(r)$	$\lvert V(r)\rvert/G(r)$
H(41F)···N(3I)	0.181(22)	2.634(15)	0.025	1.954	−0.023 (−60.386)	0.025 (65.638)	0.002 (5.251)	0.912
	0.228	2.194	0.036	1.942	−0.025 (−65.638)	0.024 (63.012)	−0.001 (−2.626)	1.044
	0.218	2.062	0.034	1.958	−0.023 (−60.386)	0.022 (57.761)	−0.001 (−2.626)	1.045
H(2NI)···N(3F)	0.161(16)	2.133(7)	0.075	2.051	−0.019 (−49.884)	0.020 (52.510)	0.002 (5.251)	0.917
	0.176	1.826	0.073	2.051	−0.017 (−44.633)	0.018 (47.259)	0.001 (2.626)	0.945
	0.164	1.779	0.080	2.075	−0.015 (−39.382)	0.016 (42.008)	0.001 (2.626)	0.938
H(3I)···O(2F)	0.072(2)	0.952(1)	0.154	2.534	−0.006 (−15.753)	0.008 (21.004)	0.002 (5.251)	0.776
	0.081	0.971	0.151	2.438	−0.007 (−18.378)	0.009 (23.630)	0.001 (2.626)	0.847
	0.071	0.823	0.141	2.506	−0.006 (−15.753)	0.007 (18.378)	0.001 (2.626)	0.857
H(1F)···O(2F)^{i}	0.322	4.037	0.027	1.696	−0.050 (−131.275)	0.046 (120.773)	−0.004 (−10.502)	1.088
	0.300	3.275	0.037	1.732	−0.041 (−107.646)	0.037 (97.144)	−0.003 (−7.876)	1.092
	-	-	-	-	-	-	-	-
H(31I)···O(1I)^{ii}	0.105	1.596	0.066	2.174	−0.011 (−28.880)	0.014 (36.757)	0.003 (7.876)	0.802
	0.121	1.704	0.053	2.097	−0.012 (−31.506)	0.015 (39.382)	0.002 (5.251)	0.830
	-	-	-	-	-	-	-	-
H(32I)···O(1I)^{iii}	0.077	1.566	0.118	2.137	−0.009 (−23.630)	0.012 (31.506)	0.004 (10.502)	0.698
	0.116	1.506	0.052	2.196	−0.012 (−31.506)	0.014 (36.757)	0.002 (5.251)	0.856
	-	-	-	-	-	-	-	-
H(42F)···N(1I)^{iv}	0.196	2.682	0.135	1.972	−0.025 (−65.638)	0.026 (68.263)	0.001 (2.626)	0.946
	0.231	2.264	0.044	1.921	−0.026 (−68.263)	0.024 (63.012)	−0.001 (−2.626)	1.044
	-	-	-	-	-	-	-	-
H(3I)···N(3F)^{v}	0.064	0.814	0.526	2.556	−0.005 (−13.128)	0.007 (18.378)	0.002 (5.251)	0.766
	0.034	0.406	0.939	2.944	−0.003 (−7.876)	0.003 (7.876)	0.001 (2.626)	0.793
	-	-	-	-	-	-	-	-
H(6F)···F(5F)^{vi}	0.047	0.790	0.161	2.422	−0.004 (−10.502)	0.006 (15.753)	0.002 (5.251)	0.676
	0.063	0.920	0.067	2.358	−0.007 (−18.378)	0.008 (21.004)	0.001 (2.626)	0.825
	-	-	-	-	-	-	-	-

[a]Electron densities are in e Å^{-3}, the Laplacian of electron densities are in e Å^{-5}, R_{ij} is in Å, and energy densities are in Hartree bohr^{-3} (values in parentheses are given in kJ mol^{-1} per atomic unit volume). Symmetry operations: (i) 1−*x*,2−*y*,−*z*; (ii) −*x*,2−*y*,1−*z*; (iii) 1−*x*, 2−*y*,1−*z*; (iv) 1+*x*,1+*y*,*z*; (v) −1+*x*,*y*,*z*; and (vi) 2−*x*,3−*y*,−*z*. Line one: model I; line two: model II, and line three: model III. (−) values are not obtainable for the gas-phase calculation (model III).

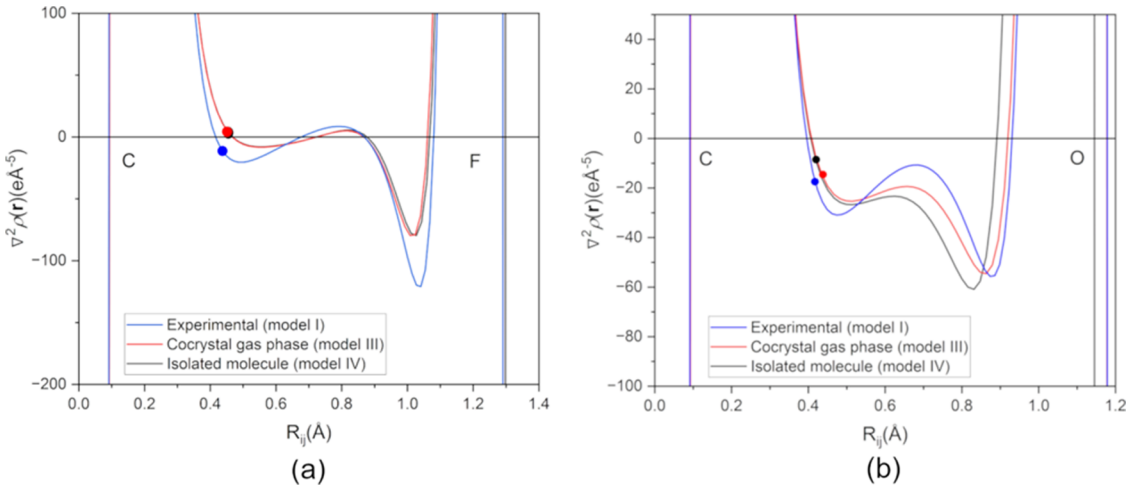

Figure 5. Laplacian profiles for (a) C−F and (b) C−O bonds in models I (blue), III (red), and IV (black). The points in the graphs represent the bond critical point positions.

A comparison between the values of the topological descriptors for the cocrystal and those for the isolated molecule, as listed in Table 3, allows some inferences to be made regarding charge redistribution upon cocrystal formation. Since the formation of the synthon involves the weakening and strengthening of certain bonds, it is possible to see that, except for N(3F)−C(2F), bonds containing atoms participating directly in H-bonds are elongated, and the electron density is diminished, namely, C(3I)−H(3I), N(2I)−H(2NI), N(2I)−N(3I), N(4F)−H(41F), N(3F)−C(4F), and O(2F)−C(2F). On the other hand, bonds present in the ring formed by the H-bonds, but not directly participating in the H-bonds, present an increase in the electron density. These bonds are C(3I)−C(4I), C(4I)−C(7I), C(7I)−N(2I), and N(4F)−C(4F). In the case of the N(3F) atom, the bond N(3F)−C(4F), participating in the 7-membered ring, presents a decrease in

https://doi.org/10.1021/acs.cgd.4c00401
Cryst. Growth Des. 2024, 24, 5614−5626

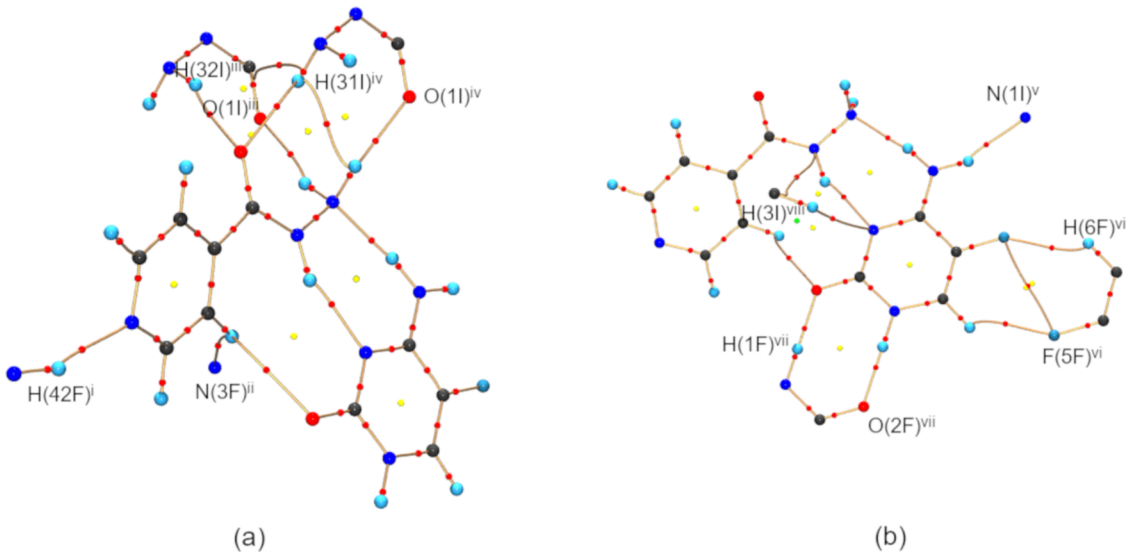

Figure 6. Molecular graph for model I showing intermolecular H-bonds involving (a) the INH molecule and (b) the 5FC molecule. Symmetry operations: (i) −1+*x*,−1+*y*,*z*; (ii) −1+*x*,*y*,*z*; (iii) −*x*,2−*y*,1−*z*; (iv) 1−*x*,2−*y*,1−*z*; (v) 1+*x*,1+*y*,*z*; (vi) 2−*x*,3−*y*,−*z*; (vii) 1−*x*,2−*y*,−*z*; and (viii) 1+*x*,*y*,*z*.

the electron density, while its other covalent bond, N(3F)−C(2F), participating in the 9-membered ring, has an increase in the electron density. Figure S6 schematically represents these variations in bond electron densities upon cocrystal formation. The comparison with the experimental topological descriptors for INH,[35] on the other hand, demonstrates that the cocrystallization process causes a decrease in the electron density for all bonds in INH, except for N(2I)−H(2NI), which has an increase in the electron density at the BCP, and for C(4I)−C(7I), which remains unaltered.

Intermolecular Interactions. Concerning the H-bonds (Table 4), it is possible to see a much lower electron density at the bond critical points when compared to the covalent bonds, along with a positive Laplacian of the electron density, indicating closed-shell interactions, as it would be expected. The H-bonds that stabilize the cocrystal consist of N−H···N and C−H···O intermolecular interactions. The interactions of the N−H···N type present low electron density values (0.181 e Å^{-3} for H(41F)···N(3I) and 0.161 e Å^{-3} for H(2NI)···N(3F)) in agreement with the theoretical models. They also have very low ellipticity, as can be seen in Table 4, for the three analyzed models. The H-bond of the C−H···O type presents an ellipticity higher than the N−H···N type but a lower electron density at the BCP. Apart from the H-bonds between the molecules in the cocrystal, other H-bonds stabilize the three-dimensional packing of the crystalline structure. These interactions are of types N−H···N, N−H···O, and C−H···F, and Figure 6 depicts the molecular graph for such interactions. As expected, the Laplacian for the H-bonds presents small positive values, thus indicating a depletion of the electron density in this region and an ionic character of these bonds (closed-shell, $\nabla^2\rho_{BCP} > 0$)[45] in all models (Table 4). However, even though the low electron density and the positive Laplacian are indicative of closed-shell interactions, further information can be obtained by analyzing the energy densities for these types of interactions. For the experimental data (model I), the energy densities were calculated following the Abramov approximation,[46] in which the electron densities at the BCP and their Laplacian are used for the calculation of the kinetic ($G(\boldsymbol{r})$) and potential ($V(\boldsymbol{r})$) energy densities. The total energy density is then obtained through the virial theorem. The calculated values are displayed in Table 4, and characterization of the H-bonds can be performed following the method proposed by Espinosa and co-workers.[47] In this sense, the negative value for the total energy density ($H(\boldsymbol{r})$) along with a ratio of the modulus of the potential to the kinetic energy density between 1 and 2 ($2 > |V(\boldsymbol{r})|/G(\boldsymbol{r}) > 1$) characterizes the interaction as in the transit region between a pure closed-shell and a pure shared-shell interaction, while the positive $H(\boldsymbol{r})$ value and $|V(\boldsymbol{r})|/G(\boldsymbol{r}) < 1$ characterize the interactions as pure closed-shell. Through Table 4, one can see that, concerning the experimental results, only the interaction H(1F)···O(2F)^{i} could be classified as in the transit region between closed-shell and shared-shell interactions, while the remaining H-bonds are all characterized as purely closed-shell interactions. Theoretically, the interaction H(41F)···N(3I) from the synthon could be classified as in the transit zone (concerning both the periodic and the gas-phase calculations) along with H(1F)···O(2F)^{i} and H(42F)···N(1I)^{iv}. However, in all cases, the total energy is very close to zero and $|V(\boldsymbol{r})|/G(\boldsymbol{r})$ close to unity, indicating that the covalent character of the interactions is minor.

Apart from H-bonds, a bond path for halogen bonding was found, characterized as the type-I F···F interaction (Figure 6b) since C−F···F and F···F−C angles are different from 180 or 90° and equal to each other,[48] presenting an electron density at the BCP of 0.023(1) e Å^{-3} and a Laplacian of 0.370(1) e Å^{-5}. This type of interaction is very common when halogen atoms are present, and it has been a source of much interest in the past years. One importance of this type of interaction concerns the role it plays in biological systems, for instance, in halogen bond-mediated transmembrane transport.[49]

Laplacian Maps. The mapping of the negative of the Laplacian is shown in Figure 7 for both experimental and theoretical periodic calculations. Figure 7 presents the contour map of the Laplacian in the plane containing the hetero-synthon, the hydrazide group belonging to INH, and the 5FC molecule, showing the regions known as the VSCC, and the presence of the electron lone pairs of N, O, and F atoms. It is possible to observe the regions of charge accumulation in

https://doi.org/10.1021/acs.cgd.4c00401
Cryst. Growth Des. 2024, 24, 5614−5626

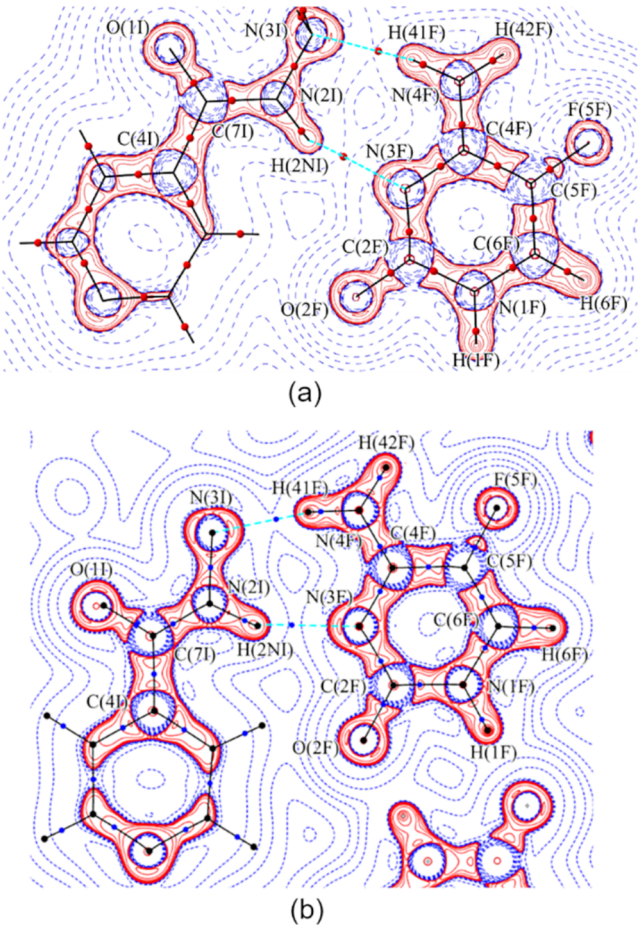

Figure 7. Mapping of the negative of the Laplacian for 5FC:INH: (a) experimental and (b) theoretical. Contours at $\pm 2^m.10^n$ e Å^{-5} (m = 1 to 3, n = −3 to 3). Red contours are positive, and blue contours are negative.

covalent bonds and lone pairs, which coincide in number and position with the Lewis pairs, indicating that the sites are available for electrophilic and nucleophilic attack, thus informing about the molecule's reactivity.[45] The map shows the alignment of the lone-pair electrons present in the acceptor N atom toward the donor H atom belonging to each of the H-bonds in the heterosynthon.

Being the most electronegative element in the periodic table, fluorine causes a very peculiar distribution of the electron density in the C−F bond, as seen by the Laplacian map. It is possible to observe the region in the C(5F)−F(5F) bond where the VSCC closest to the C atom presents a small conical shape, as described previously by Murgich and co-workers[41] for this bond in the gas-phase calculation of 5FC. It is also possible to see that the BCP for the C−F bond lies in a region closer to the C atom than its VSCC, so both VSCCs belong to the atomic basin of the F atom, as already discussed. The VSCCs around the F atom form a nearly spherical shape, presenting edges corresponding to the lone pairs. The plotting of the Laplacian isosurface highlights this feature (Figure S8).

The high polarization between carbon and fluorine in the C−F bond behaves as a very stable dipole due to the electronegativity of fluorine, diminishing the covalent character of this bond.[50,51] The three lone pairs of the F atom are held together by the electronegativity of fluorine and the adjacent partially charged carbon atoms, so the F atom interacts with its environment in a more electrostatic manner.[51]

Atomic Charges. The atomic charges were calculated according to QTAIM through the integration of the electron density inside the atomic basins. The obtained values are displayed in Table 5. The comparison between models I and III (considering the cocrystal) and model IV (isolated molecules) allows further understanding of the charge redistribution upon cocrystallization.

Table 5. Atomic Charges Calculated through the QTAIM[a]

atom	charge (e)	volume (Å^3)	atom	charge (e)	volume (Å^3)
F(5F)	−0.4811	16.356	N(2I)	−1.2272	13.198
	−0.6185	15.963		−0.8534	13.522
	−0.6184	16.073		−0.7771	13.494
O(2F)	−1.2271	17.008	N(3I)	−0.6370	14.655
	−1.1380	20.403		−0.6482	14.406
	−1.1512	20.604		−0.6202	16.235
N(1F)	−1.7838	15.727	C(2I)	0.6332	11.022
	−1.1574	14.289		0.5287	10.493
	−1.1115	14.410		0.5195	10.555
N(3F)	−1.0709	13.850	C(3I)	−0.0886	11.137
	−1.0996	16.062		−0.0163	12.041
	−1.0919	17.727		−0.0340	12.366
N(4F)	−1.3589	17.551	C(4I)	−0.3720	9.864
	−1.1843	17.198		−0.0232	10.584
	−1.1262	17.321		−0.0241	10.628
C(2F)	2.2911	3.386	C(5I)	−0.3053	12.351
	1.7340	5.150		−0.0116	12.165
	1.7232	5.268		−0.0094	12.231
C(4F)	1.3765	5.739	C(6I)	0.4428	11.342
	1.0675	6.774		0.4996	10.670
	1.0741	6.829		0.5110	10.599
C(5F)	0.4688	8.754	C(7I)	1.7277	4.815
	0.4836	9.587		1.3912	6.070
	0.4688	9.732		1.3734	6.171
C(6F)	0.8484	9.611	H(2I)	0.1703	6.949
	0.4765	10.474		0.0426	7.198
	0.4810	10.487		0.0391	7.174
H(1F)	0.4487	2.892	H(3I)	0.1853	4.411
	0.4341	4.223		0.0705	6.072
	0.4209	4.337		0.0314	7.045
H(6F)	0.1269	6.861	H(5I)	0.1230	5.664
	0.0944	6.711		0.0638	6.755
	0.0884	6.767		0.0722	6.739
H(41F)	0.4904	2.900	H(6I)	0.1991	6.787
	0.4844	2.810		0.0312	7.254
	0.4240	4.317		0.0419	7.147
H(42F)	0.4497	2.717	H(31I)	0.4507	2.824
	0.4131	4.186		0.3683	4.664
	0.4187	4.164		0.3687	4.574
O(1I)	−0.9790	17.520	H(32I)	0.4798	3.102
	−1.1439	19.965		0.3602	4.808
	−1.1387	19.828		0.3532	4.851
N(1I)	−1.7909	16.502	H(2NI)	0.4573	2.745
	−1.1179	18.056		0.4686	2.898
	−1.1026	17.944		0.3958	4.400
			∑cocrystal	0.048	278.239
				0.000	301.451

[a]First line: model I, second line: model III, and third line: model IV.

https://doi.org/10.1021/acs.cgd.4c00401
Cryst. Growth Des. 2024, 24, 5614−5626

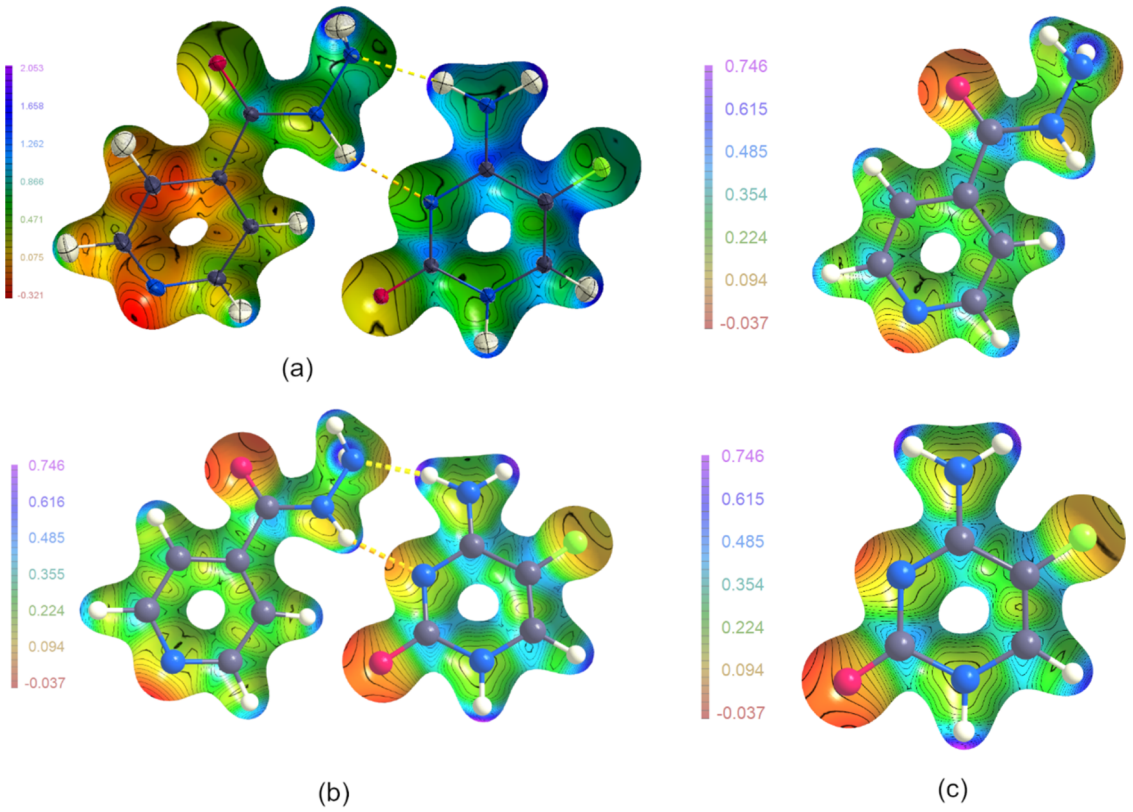

Figure 8. Electrostatic potential mapping for (a) experimental data (model I), (b) theoretical data considering the cocrystal (model III), and (c) isolated INH and 5FC molecules (model IV). Isosurfaces are at 0.5 e Å^{-3}.

The atomic charges calculated by the QTAIM present reasonable values, with negative charges being mostly related to N, O, and F atoms and positive charges being related to C and H atoms. The exceptions are C atoms from the INH ring, which present slightly negative charges. However, these charges are very small and are close to neutrality. The total charge of the cocrystal close to zero and the total volume for the experimental model close to half of the unit cell volume also indicate that the atomic charges and volumes were properly calculated.

The comparison between the cocrystal and the isolated molecules in the gas phase reveals some expected changes. The main variations concern the decrease in atomic volumes for the atoms participating in the heterosynthon, in comparison to the isolated molecules. Atoms N(3I) and H(41F), for instance, decrease more than 50% in the basin volume. The differences in charges, on the other hand, are not so pronounced. The highest charge variations are related to the H atom involved in H-bonds in the cocrystal, becoming more positive upon interaction. But overall, it is possible to observe an increase in the negative charge for all N atoms, except N(3F), and an increase in the negative charge for O(2F). In addition, while the charges of C atoms from the 5FC ring become more positive, the charges for C atoms in the INH ring become less positive. Possibly, in the case of the 5FC ring, the electrons are being drawn by O(2F), N(1F), and N(4F), while in the case of INH, the electrons are being drawn by the pyridine ring. Also, the redistribution of charge happens from the 5FC molecule to INH since the latter presents a total charge of approximately −0.53 e in the cocrystal and the former presents a total charge of approximately +0.58 e in the cocrystal for model I (experimental), while for model III, in which the cocrystal was considered in the gas phase, the 5FC molecule presents a charge of −0.01 and the INH molecule presents a charge of +0.01, being practically neutral. However, the theoretically obtained delocalization indices indicate electron sharing between the atoms involved in H-bonds (Table S4).

Electrostatic Potential Mapping. The electrostatic potential was calculated for the 5FC:INH cocrystal, mapped onto the electron density isosurface, determined by model I, as illustrated in Figure 8a. The map was also calculated for models III and IV for comparison (Figure 8b,c). The mapping of the electrostatic potential allows observation of the electronegative and electropositive regions, giving insights about the reactivity of compounds. The electronegative regions are known as sites of protonation and nucleophilic attacks and are thus related to pharmaceutical properties. In the case of the cocrystals under study, they are depicted in the vicinity of the atoms belonging to the pyridine ring of INH and the atoms of O(1I), O(2F), N(2I), and N(3F). On the other hand, electropositive regions can be seen at the pyrimidine ring of 5FC and in the vicinity of the H(2NI) and H(41F) atoms, which are also involved in the formation of the heterosynthon. This is in agreement with the variations in atomic charge observed when the cocrystal is formed in which the pyridine ring of INH becomes more negative and the pyrimidine ring of 5FC becomes more positive. A region with a slightly neutral value of the electrostatic potential is observed on the surface of the F atom, while the surroundings have a more negative potential, indicating some degree of σ effect on the C−F bond

https://doi.org/10.1021/acs.cgd.4c00401
Cryst. Growth Des. 2024, 24, 5614−5626

(Figure S9), which corroborates with the weak F···H and F···F interactions already discussed.

Interestingly, in the charge density study performed by Rajalakshmi and co-workers[35] on the INH molecule, the electrostatic potential for the molecule indicated that the N(3I) atom was a possible reaction site for hydrogen bonds due to its electronegativity, along with O(1I) and N(1I). Upon the formation of the cocrystal, the N(3I) atom becomes less electronegative, with a nearly neutral electrostatic potential, while N(2I) becomes more electronegative in comparison to its behavior in the pure INH molecule.[35]

Comparing the mapping of the electrostatic potential for models III and IV (Figure 8b,c), it is possible to observe subtle variations in the electrostatic potential for the molecules in the cocrystal (Figure 8b) in relation to the individual molecules (Figure 8c). For instance, the potential for the N atom from the 5FC molecule involved in the synthon H-bond becomes less negative in the cocrystal. In addition, a comparison between the theoretical models and the experiment shows that the F atom has a slight negative potential in the theoretical data, in contrast with the near neutral potential for the F atom in the experiment. The N(3F) and O(2F) atoms involved in the synthon H-bonds also present a more negative potential in the theoretical models.

CONCLUSIONS

Through charge density and topological analyses, the electronic features of the 5FC:INH cocrystal could be explored, allowing a comparison with the theoretical isolated molecules and with the experimental charge density for INH.[35] In this way, some inferences regarding charge redistribution could be done.

The analysis of the intermolecular interactions showed that most H-bonds in the crystalline structure are electrostatic in nature, with a very small covalent character for H(1F)···O(2F)^{i} (experimentally) and for the H-bonds from the synthon (theoretically). Furthermore, a F···F halogen bond was found, which is of relevance in biological systems.

The mapping of the electrostatic potential agrees with the inferred charge redistribution in the cocrystallization process, indicating a more negative potential for the INH ring and a more positive potential for the 5FC ring.

ASSOCIATED CONTENT

Supporting Information

The Supporting Information is available free of charge at https://pubs.acs.org/doi/10.1021/acs.cgd.4c00401.

Refinement parameters (Hirshfeld rigid bond test, graphs for refinement statistics, statistics for different conditions on the reflection threshold); three-dimensional packing stabilized by H-bonds, full topological descriptors for bond critical points, figures for gradient trajectories of the electron density, comparison of the electron density and Laplacian of the electron density at the bond critical points for all models, schematic representation on the variation of the electron density upon cocrystallization, delocalization indexes for intermolecular interactions, figures of the negative Laplacian of the electron density for the periodic calculations, Laplacian isosurface highlighting the F atom, and the electrostatic potential map highlighting the F atom; file containing the .fco from XD refinement (PDF)

Refined data (PDF)

Accession Codes

CCDC 2340078−2340079 contain the supplementary crystallographic data for this paper. These data can be obtained free of charge via www.ccdc.cam.ac.uk/data_request/cif, by emailing at data_request@ccdc.cam.ac.uk, or by contacting the Cambridge Crystallographic Data Centre, 12 Union Road, Cambridge CB2 1EZ, UK; fax: +44 1223 336033.

AUTHOR INFORMATION

Corresponding Author

Javier Ellena − *Instituto de Física de São Carlos − Universidade de São Paulo, 13566-590 São Carlos, SP, Brazil*; orcid.org/0000-0002-0676-3098; Email: javiere@ifsc.usp.br

Authors

Camila B. Pinto − *Instituto de Física de São Carlos − Universidade de São Paulo, 13566-590 São Carlos, SP, Brazil*

Adilson B. Wanderley − *Instituto de Física de São Carlos − Universidade de São Paulo, 13566-590 São Carlos, SP, Brazil*

Juan C. Tenorio − *Instituto de Física − Universidade Federal do Rio de Janeiro, 21941-909 Rio de Janeiro, RJ, Brazil; Max-Planck-Institut für Kohlenforschung, 45470 Mülheim a.d Ruhr, Germany*

Ihosvany Camps − *Departamento de Física, Instituto de Cîencias Exatas, Universidade Federal de Alfenas, 37133-840 Alfenas, MG, Brazil*

Christian W. Lehmann − *Max-Planck-Institut für Kohlenforschung, 45470 Mülheim a.d Ruhr, Germany*

Complete contact information is available at: https://pubs.acs.org/10.1021/acs.cgd.4c00401

Funding

The Article Processing Charge for the publication of this research was funded by the Coordination for the Improvement of Higher Education Personnel - CAPES (ROR identifier: 00x0ma614).

Notes

The authors declare no competing financial interest.

ACKNOWLEDGMENTS

The authors are grateful to the Brazilian funding agencies FAPESP (2013/07581-9, 2016/08823-4, 2017/15850-0, and 2023/10889-7) and CNPq (312505/2021-3). This study was financed in part by the Coordenação de Aperfeiçoamento de Pessoal de Nível Superior−Brasil (CAPES)−Finance code 001. The authors thank the scientific staff from the Chemical Crystallography and Electron Microscopy Department of the Max-Planck-Institut für Kohlenforschung, especially Dr. Richard Goddard and Angelika Dreier for support during the experimental measurements. We also thank Matheus da Silva Souza for providing the crystals used in the X-ray diffraction experiments and Lucas Militão for helping with computational details.

REFERENCES

(1) Wouters, J.; Quere, L.; Thurston, D. E. *Pharmaceutical Salts and Co-crystals*; Royal Society of Chemistry, 2011.

(2) Nicolaï, B.; Fournier, B.; Dahaoui, S.; Gillet, J.-M.; Ghermani, N.-E. Crystal and electron properties of carbamazepine-aspirin co-crystal. *Cryst. Growth Des.* **2019**, *19*, 1308−1321.
(3) Zhang, C.; Xiong, Y.; Jiao, F.; Wang, M.; Li, H. Redefining the term of "cocrystal" and broadening its intention. *Cryst. Growth Des.* **2019**, *19*, 1471−1478.
(4) Desiraju, G. R. Supramolecular synthons in crystal engineering − a new organic synthesis. *Angew. Chem., Int. Ed.* **1995**, *34*, 2311−2327.
(5) Dai, X.-L.; Chen, J.-M.; Lu, T.-B. Pharmaceutical cocrystallization: an effective approach to modulate the physicochemical properties of solid-state drugs. *CrystEngComm* **2018**, *20*, 5292−5316.
(6) Bordignon, S.; Vioglio, P. C.; Priola, E.; Voinovich, D.; Gobetto, R.; Nishiyama, Y.; Chierotti, M. R. Engineering codrug solid forms: mechanochemical synthesis of an indomethacin-caffeine system. *Cryst. Growth Des.* **2017**, *17* (11), 5744−5752.
(7) Souza, M. S.; Diniz, L. F.; Vogt, L.; Carvalho, P. S., Jr.; D'vries, R. F.; Ellena, J. Mechanochemical Synthesis of a multicomponent solid form: the case of 5-fluorocytosine isoniazid codrug. *Cryst. Growth Des.* **2018**, *18*, 5202−5209.
(8) Takayama, K.; Wang, L.; David, H. L. Effect of isoniazid on the in vivo mycolic acid synthesis, cell growth, and viability of *Mycobacterium tuberculosis*. *Antimicrob. Agents Chemother.* **1972**, *2*, 29−35.
(9) Tassel, D.; Madoff, M. A. Treatment of candida sepsis and cryptococcus meningitis with 5-fluorocytosine. *JAMA* **1968**, *206* (4), 830−832.
(10) Etter, M. C. Encoding and decoding hydrogen-bond patterns of organic compounds. *Acc. Chem. Res.* **1990**, *23*, 120−126.
(11) Bader, R. F. W. *Atoms in Molecules: A Quantum Theory*; Oxford University Press: Oxford, U. K., 1990.
(12) Bruker. *Apex2, Saint and SADABS*; Bruker AXS Inc.: Madinson, Wisconsin, USA, 2010.
(13) Sheldrick, G. M. *SHELXS-97: Program for Crystal Structure Resolution*; University of Göttingen: Göttingen, Germany, 1997.
(14) Sheldrick, G. M. A short history of SHELX. *Acta Crystallogr., Sect. A: Found. Crystallogr.* **2008**, *64*, 112−122.
(15) Dolomanov, O. V.; Bourhis, L. J.; Gildea, R. J.; Howard, J. A. K.; Puschmann, H. Olex2: A complete structure solution, refinement and analysis program. *J. Appl. Crystallogr.* **2009**, *42*, 339−341.
(16) Farrugia, L. J. WinGX and ORTEP for Windows: an update. *J. Appl. Crystallogr.* **2012**, *45*, 849−854.
(17) Hübschle, C. B.; Sheldrick, G. M.; Dittrich, B. ShelXle: a Qt graphical user interface for SHELXL. *J. Appl. Crystallogr.* **2011**, *44*, 1281−1284.
(18) Hansen, N. K.; Coppens, P. Testing aspherical atom refinements on small-molecule data sets. *Acta Crystallogr., Sect. A: Found. Crystallogr.* **1978**, *34*, 909−921.
(19) Volkov, A.; Macchi, P.; Farrugia, L. J.; Gatti, C.; Mallinson, P.; Richter, T.; Koritsanszky, T. *XD2006 − A computer program package for multipole refinement, topological analysis, of charge densities and evaluation of intermolecular interaction energies from experimental and theoretical structure factors*. University of Buffalo, State University of New York, NY, USA; University of Milano, Italy; University of Glasgow, UK; CNRISTM, Milano, Italy, Middle Tennessee State University, TN, USA, 2006.
(20) Madsen, A. s. SHADE web server for estimation of hydrogen anisotropic displacement parameters. *J. Appl. Crystallogr.* **2006**, *39*, 757−758.
(21) Munshi, P.; Madsen, A. Ø.; Spackman, M. A.; Larsen, S.; Destro, R. Estimated H-atom anisotropic displacement parameters: a comparison between different methods and with neutron diffraction results. *Acta Crystallogr., Sect. A: Found. Crystallogr.* **2008**, *64*, 465−475.
(22) Allen, F. H.; Bruno, I. J. Bond lengths in organic and metal-organic compounds revisited: X−H bond lengths from neutron diffraction data. *Acta Crystallogr., Sect. B: Struct. Sci., Cryst. Eng. Mater.* **2010**, *66*, 380−386.
(23) Volkov, A.; Abramov, Y. A.; Coppens, P. Density-optimized radial exponents for X-ray charge-density refinement from ab initio crystal calculations. *Acta Crystallogr., Sect. A: Found. Crystallogr.* **2001**, *57*, 272−282.
(24) Zhurov, V. V.; Zhurova, E. A.; Pinkerton, A. A. Optimization and evaluation of data quality for charge density studies. *J. Appl. Crystallogr.* **2008**, *41*, 340−349.
(25) Meindl, K.; Henn, J. Foundations of residual-density analysis. *Acta Crystallogr., Sect. A: Found. Crystallogr.* **2008**, *64*, 404−418.
(26) Hübschle, C. B.; Dittrich, B. MoleCoolQt − a molecule viewer for charge-density research. *J. Appl. Crystallogr.* **2011**, *44*, 238−240.
(27) Dovesi, R.; Orlando, R.; Erba, A.; Zicovich-Wilson, C. M.; Civalleri, B.; Casassa, S.; Maschio, L.; Ferrabone, M.; De La Pierre, M.; D'Arco, P.; Noel, Y.; Causa, M.; Rerat, M.; Kirtman, B. CRYSTAL14: A program for the ab initio investigation of crystalline solids. *Int. J. Quantum Chem.* **2014**, *114*, 1287−1317.
(28) Becke, A. D. Density-functional thermochemistry. I. The effect of the exchange-only gradient correction. *J. Chem. Phys.* **1992**, *96*, 2155−2160.
(29) Lee, C.; Yang, W.; Parr, R. G. Development of the Colle-Salvetti correlation-energy formula into a functional of the electron density. *Phys. Rev. B* **1988**, *37*, 785.
(30) Frisch, M. J.; Trucks, G. W.; Schlegel, H. B.; Scuseria, G. E.; Robb, M. A.; Cheeseman, J. R.; Scalmani, G.; Barone, V.; Petersson, G. A.; Nakatsuji, H.; Li, X.; Caricato, M.; Marenich, A.; Bloino, J.; Janesko, B. G.et al. *Gaussian 09*; Gaussian, Inc.: Wallingford CT, 2016.
(31) Gatti, C. TOPOND-96: An electron density topological program for systems periodic in N (N = 0−3) dimensions. In *User's Manual*; CNR-CSRSRC: Milano, 1996.
(32) Lu, T.; Chen, F. Multiwfn: A multifunctional wavefunction analyzer. *J. Comput. Chem.* **2012**, *33*, 580−592.
(33) Keith, T. A. *AIMAll TK Gristmill Software* Overland Park, KS, 2017.
(34) Zhang, J.; Lu, T. Efficient evaluation of electrostatic potential with computerized optimized code. *Phys. Chem. Chem. Phys.* **2021**, *23*, 20323.
(35) Rajalakshmi, G.; Hathwar, V. R.; Kumaradhas, P. Topological analysis of electron density and the electrostatic properties of isoniazid: an experimental and theoretical study. *Acta Crystallogr., Sect. B: Struct. Sci., Cryst. Eng. Mater.* **2014**, *70*, 331−341.
(36) Hathwar, V. R.; Thakur, T. S.; Dubey, R.; Pavan, M. S.; Guru Row, T. N.; Desiraju, G. R. Extending the supramolecular synthon based fragment approach (SBFA) for transferability of multipole charge density parameters to monofluorobenzoic acids and their cocrystals with isonicotinamide: Importance of C−H···O, C−H···F, and F···F intermolecular regions. *J. Phys. Chem. A* **2011**, *115*, 12852−12863.
(37) Bach, A.; Lentz, D.; Luger, P. Charge density and topological analysis of pentafluorobenzoic acid. *J. Phys. Chem. A* **2001**, *105*, 7405−7412.
(38) Cheeseman, J. R.; Carroll, M. T.; Bader, R. F. W. The mechanics of hydrogen bond formation in conjugated systems. *Chem. Phys. Lett.* **1988**, *143* (5), 450−458.
(39) Koritsanszky, T. S.; Coppens, P. Chemical applications of X-ray charge-density analysis. *Chem. Rev.* **2001**, *101*, 1583−1627.
(40) Rajalakshmi, G.; Devipriya, B.; Parameswari, A. R.; Stephen, A. D.; Kumaradhas, P. Understanding the N−N cleavage and the electrostatic properties of isoniazid drug molecule via theoretical charge density study. *Comput. Theor. Chem.* **2011**, *966*, 259−264.
(41) Murgich, J.; Franco, H. J.; San-Blas, G. Topology of charge density of flucytosine and related molecules and characteristics of their bond charge distributions. *J. Phys. Chem. A* **2006**, *110*, 10106−10115.
(42) Hibbs, D. E.; Overgaard, J.; Piltz, R. O. X−N charge density analysis of the hydrogen bonding motif in 1-(2-hydroxy-5-nitrophenyl)ethanone. *Org. Biomol. Chem.* **2003**, *1*, 1191−1198.
(43) Jarzembska, K. N.; Kamiński, R.; Dobrzycki, Ł.; Cyrański, M. K. First experimental charge density study using a Bruker CMOS-type PHOTON 100 detector: the case of ammonium tetraoxalate

https://doi.org/10.1021/acs.cgd.4c00401
Cryst. Growth Des. 2024, 24, 5614−5626

dihydrate. *Acta Crystallogr., Sect. B: Struct. Sci., Cryst. Eng. Mater.* **2014**, *70*, 847−855.
(44) Macchi, P.; Proserpio, D. M.; Sironi, A. Experimental electron density in a transition metal dimer: metal−metal and metal−ligand bonds. *J. Am. Chem. Soc.* **1998**, *120*, 13429−13435.
(45) Bader, R. F. W. A quantum theory of molecular structure and its applications. *Chem. Rev.* **1991**, *91*, 893−928.
(46) Abramov, Y. A. On the possibility of kinetic energy density evaluation from the experimental electron-density distribution. *Acta Crystallogr., Sect. A: Found. Crystallogr.* **1997**, *53*, 264−272.
(47) Espinosa, E.; Alkorta, I.; Elguero, J.; Molins, E. From weak to strong interactions: A comprehensive analysis of the topological and energetic properties of the electron density distribution involving X−H ···F−Y systems. *J. Chem. Phys.* **2002**, *117*, 5529.
(48) Desiraju, G. R.; Parthasarathy, R. The nature of halogen··· halogen interactions: are short halogen contacts due to specific attractive forces or due to close packing of nonspherical atoms? *J. Am. Chem. Soc.* **1989**, *111*, 8725−8726.
(49) Berger, G.; Frangville, P.; Meyer, F. Halogen bonding for molecular recognition: new developments in materials and biological sciences. *Chem. Commun.* **2020**, *56*, 4970−4981.
(50) Chopra, D.; Row, T. N. G. Role of organic fluorine in crystal engineering. *CrystEngComm* **2011**, *13*, 2175.
(51) O'Hagan, D. Understanding organofluorine chemistry. An introduction to the C−F bond. *Chem. Soc. Rev.* **2008**, *37*, 308−319.

https://doi.org/10.1021/acs.cgd.4c00401
Cryst. Growth Des. 2024, 24, 5614−5626